

# Effect of Vaporization Temperature on the Diameter and Chiral Angle Distributions of Single-Walled Carbon Nanotubes

Pavel Nikolaev<sup>1,\*</sup>, William Holmes<sup>1,†</sup>, Edward Sosa<sup>1</sup>, Peter Boul<sup>1</sup>,  
Sivaram Arepalli<sup>1,†</sup>, and Leonard Yowell<sup>2</sup>

<sup>1</sup>ERC Inc. / NASA Johnson Space Center, Mail Stop ES-4, P.O.Box 58561, Houston, TX 77258, USA

<sup>2</sup>NASA Johnson Space Center, Mail Stop ES-4, P.O.Box 58561, Houston, TX 77258, USA

Pulsed laser vaporization synthesis of single-wall carbon nanotubes on Co/Ni and Rh/Pd catalysts was explored with respect to variations in the production temperature. The nanotube type populations were determined via photoluminescence, UV-Vis-NIR absorption and Raman spectroscopy. It was found that lowered production temperature leads to smaller nanotube diameters and exceptionally narrow  $(n, m)$  type distributions, with marked preference towards large chiral angles for both catalysts. Interestingly, larger nanotube diameters tend to be associated with larger chiral angles. These results demonstrate that PLV production technique can provide at least partial control over the nanotube  $(n, m)$  populations. In addition, these results have implications for the understanding the nanotube nucleation mechanism in the laser oven. SWCNT synthesized at lower temperatures appear quite attractive as a starting material for nanotube type separation experiments.

**Keywords:** Carbon, Nanotubes, Laser Ablation, Synthesis, Chiral Angle, Diameter Mechanism.

## 1. INTRODUCTION

Like with other nanomaterials, the electronic properties of single-wall carbon nanotubes (SWCNT) strongly depend on their size and molecular structure. SWCNT structure can be conveniently expressed in terms of chiral indices  $n$  and  $m$  when SWCNT is visualized as a rolled-up graphene sheet. The circumference of the SWCNT is determined by its chiral vector  $\mathbf{C}_h = n\mathbf{a}_1 + m\mathbf{a}_2$ , where  $\mathbf{a}_1$  and  $\mathbf{a}_2$  are the unit vectors of the graphene lattice, and integers  $(n, m)$  are the chiral indices. Nanotubes with  $n = m$  (armchair nanotubes) are metallic at room temperature while those with  $n - m = 3j$ , (where  $j = 1, 2, 3, \dots$ ) are strictly semi-metals, but often called metals along with armchairs. Nanotubes with  $n - m = 3j + 1$  and  $n - m = 3j + 2$  (where  $j = 0, 1, 2, 3, \dots$ ) are semiconductors with a band gap that varies approximately inversely with diameter. Metallic and

semi-metallic nanotubes exhibit singularities in the electron density of states similar to semiconducting ones, with corresponding optical transition energies inversely proportional to the diameter.

Such wealth of available electronic properties presents many opportunities to utilize SWCNTs in various applications, such as field emission sources, transistors, interconnects on microchips, conductive transparent films, photovoltaics, etc.<sup>1-6</sup> Most of these applications will benefit from use of certain  $(n, m)$  nanotube types (metallic, small gap semiconductor, etc.) However, as produced SWCNT samples are polydisperse, with many  $(n, m)$  types present and typical  $\sim 1:2$  metal/semiconductor ratio. This lack of specificity in the SWCNT samples is one of the primary reasons why SWCNTs are rarely used in commercial applications today.

The most common means of synthesizing SWCNTs include laser ablation,<sup>7</sup> arc discharge<sup>8</sup> and chemical vapor deposition (CVD) including HiPco,<sup>9</sup> CoMoCat<sup>10</sup> and alcohol CVD.<sup>11</sup> The polydispersity of nanotube populations is usually expressed in terms of diameter distributions, typically  $1.4 \pm 0.4$  nm for laser SWCNTs,<sup>12</sup>  $1.6 \pm 0.5$  nm for arc-discharge SWCNTs,<sup>13</sup> and  $1.0 \pm 0.3$  nm for HiPco SWCNTs.<sup>9,14</sup> In order to fully describe a population of nanotubes in a sample, chiral angle distributions have

\*Author to whom correspondence should be addressed.

<sup>†</sup>Present address: Department of Energy Science, Sungkyunkwan University, 300 Cheoncheon-dong, Jangan-gu, Suwon, Gyeonggi-do 440-746, Korea.

<sup>‡</sup>Present address: Alan G. MacDiarmid NanoTech Institute, The University of Texas at Dallas, 800 West Campbell Road, Richardson, TX 75080, USA.

also been utilized.<sup>15</sup> Due to a discreet nature of relationship between atomic structure and electronic properties of SWCNTs, the best way to describe a nanotube population is to determine the fraction of each  $(n, m)$  type present in a sample. Experimental methods for determining nanotube type populations include optical spectroscopy (optical absorption, photoluminescence and Raman spectroscopy) and microscopy (electron beam diffraction and scanning tunneling microscopy). For example, 33 semiconducting nanotube types have been identified in standard HiPco SWCNT samples by photoluminescence.<sup>15</sup>

There has been significant progress recently in separation of SWCNTs by type, in order to create monodispersed samples suitable for various applications [Ref. [16] and references therein]. In particular, it was discovered that nanotubes can be separated by density gradient centrifugation,<sup>17–19</sup> based on small variations in the buoyant density of surfactant-coated species. Other promising techniques rely on sidewall chemical reactions selective towards metallic tubes,<sup>20</sup> selective adsorption of solubilizing agents such as flavine<sup>21</sup> or DNA<sup>22, 23</sup> selective adsorption of semiconducting nanotubes on agarose gel<sup>24, 25</sup> and dielectrophoresis in a flow channel,<sup>26, 27</sup> the latter two techniques being quite amenable for scale-up. However, selectivity, reproducibility, and scalability of all approaches to nanotube type separation have much room for improvement, as the techniques are still in their infancy.

The production of SWCNTs with narrow “tube type populations” might be beneficial for the subsequent separation efforts, especially since most techniques only separate metallic tubes from semiconducting ones, and further separation by band gap and/or chiral angle is more complicated. However, there are only few reports on production of nanotube samples enriched in certain nanotube types. The best known example are low temperature CoMoCat SWCNTs,<sup>10</sup> that are naturally enriched in  $(6, 5)$ ,  $(7, 5)$  and  $(7, 6)$  types. SWCNTs produced by alcohol CVD technique<sup>11</sup> at lower temperatures are similarly enriched in the  $(6, 5)$ ,  $(7, 5)$  and  $(7, 6)$  types. SWCNT samples enriched in  $(7, 6)$  type were also produced by pulsed laser vaporization (PLV) technique on Rh/Pd catalyst.<sup>28</sup> Unfortunately, use of Rh/Pd catalyst increases cost and reduces nanotube yield.

In the present work, PLV production of SWCNTs on Co/Ni and Rh/Pd catalyst was explored with respect to variations in the production temperature. In case of Co/Ni catalyst, the temperature was lowered with respect to the standard 1200 °C,<sup>29–32</sup> while for Rh/Pd catalyst the temperature was varied around 1150 °C reported in Ref. [28]. The nanotube type populations were determined via photoluminescence (PL), UV-Vis-NIR absorption and Raman spectroscopy. A reduction in the average diameter of PLV nanotubes at lowered production temperature has long been known to occur.<sup>12, 29</sup> The effect of the pressure and carrier gas (Ar and He) on the populations of the semiconducting nanotubes has been studied in Ref. [33], with

reported predominance of type II tubes and shift away from close-to-armchair structures at higher pressure and in He carrier gas. However, the temperature effect on nanotube population (and not just diameters) has not been explored.

## 2. EXPERIMENTAL DETAILS

Single-wall carbon nanotubes were produced in the PLV setup at NASA Johnson Space Center described elsewhere<sup>29–32</sup> at the following conditions:

(1) Co/Ni catalyst (1 at.% each). Argon buffer gas at 500 Torr pressure and 100 sccm flow rate. Green/IR ablation laser combination (2nd and 1st harmonics of Nd:YAG lasers) with 50 ns pulse delay, 1.6 J/cm<sup>2</sup> energy density each and 60 Hz repetition rate. Three operating temperatures were selected: 900, 1000 and 1100 °C. Each run lasted 1 hour.

(2) Rh/Pd catalyst (1 at.% each). Argon buffer gas at 750 Torr pressure and 100 sccm flow rate, Green/IR ablation laser combination with 50 ns pulse delay, 1.6 J/cm<sup>2</sup> energy density each and 10 Hz repetition rate. Three operating temperatures were selected: 1100, 1150 and 1200 °C. The increased pressure and decreased laser repetition rate were selected according to Ref. [28]. Each run lasted 3.5 hours.

The samples were collected from the PLV setup and dispersed in D<sub>2</sub>O/1.5% SDBS (surfactant) by ultrasonication at ~1 mg/ml concentration. The resulting dispersions were centrifuged at 74,000 g for 2 hrs. The top 2/3rd of the resulting supernatant was separated and used for photoluminescence and absorption spectroscopy measurements. Photoluminescence (PL) spectra in the 800–1600 nm range were collected with 659 and 784 nm excitations on Nanospectralyzer (Applied Nanofluorescence, Houston, TX). Absorption spectra were collected on Perkin Elmer Lambda 900 spectrometer in the 325–1600 nm range. Raman spectra were acquired with 514, 633 and 785 nm excitations on dry nanotubes using Renishaw inVia spectrometer.

## 3. RESULTS AND DISCUSSION

Absorption spectra of three Co/Ni samples and three Rh/Pd samples are shown on Figures 1 and 2. Metallic M<sub>11</sub> transitions are marked in red, semiconducting S<sub>22</sub> transitions in blue and semiconducting S<sub>11</sub> transitions in black. The intensity of the spectral features with respect to background implies that SWCNT purity in Rh/Pd samples is smaller compared to Co/Ni catalyst, and decreases strongly with decrease in the temperature. Similar decrease in purity at lower temperature is present in the Co/Ni samples, but is much less pronounced. Average diameters and widths of diameter distributions increase as the temperature is increased.

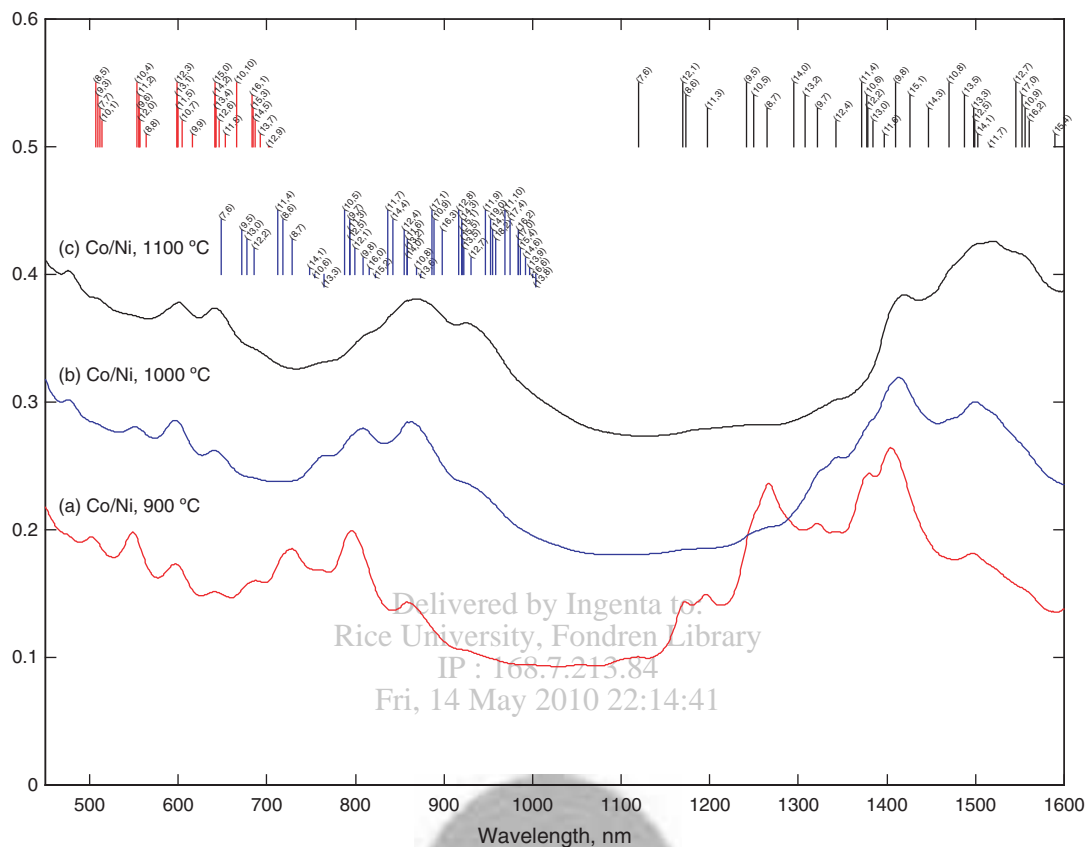


**Fig. 1.** UV-Vis-NIR absorption spectra of SWCNT samples produced on Co/Ni catalyst at (a) 900 °C, (b) 1000 °C and (c) 1100 °C. Metallic  $M_{11}$  transition are marked in red, semiconducting  $S_{22}$  in blue and  $S_{11}$  in black.

PL spectra of all samples are shown on Figures 3–8. The  $S_{11}$  emission frequencies of the semiconducting nanotubes are marked on top. Again, it can be seen that the average diameters and widths of diameter distributions increase as the temperature is increased for both catalysts. The range of the spectral features observed on the 900 °C Co/Ni sample is the narrowest. As the diameters of the nanotubes increase at higher temperatures, the emission wavelengths of the large diameter nanotubes present in 1000 and 1100 °C Co/Ni samples obviously exceed the range of the instrument. However, for Rh/Pd samples the emission is within the detector range for all samples.

Raman radial breathing mode (RBM) spectra of all samples are shown on Figures 9 and 10. Nanotube types that can be assigned to particular peaks are marked on top (metallic in red and semiconducting in black). Only few nanotube types are in the resonance with each excitation laser, which has a strong effect on the Raman RBM spectra. For example, 514 nm excitation spectra of the Co/Ni samples (Fig. 9) are dominated by contribution from only three large diameter semiconducting SWCNTs resonant on  $S_{33}$  transitions, with small contribution from three small diameter metallic nanotubes. 633 nm excitation spectra of these samples are almost exclusively dominated by metallic nanotubes, and 785 nm excitation spectra show

exclusively semiconducting SWCNT features. For Rh/Pd samples, 514 nm excitation spectra only show metallic nanotubes, 633 nm excitation spectra are split in half among large metallic and small semiconducting tubes, and 785 nm excitation spectra only show semiconducting nanotubes.

The  $(n, m)$  population analysis employed the strategy proposed first in Ref. [10]. Interband transition energies and Raman RBM frequencies were tabulated according to Ref. [34, 35]. A preliminary graphene sheet plot for the sample was constructed according to the PL data. Then for each semiconducting nanotube  $(n, m)$  type, its presence was checked in the PL, absorption and Raman spectra, taking into account how far it is from the resonance with excitation lasers in case of emission and Raman spectra. After semiconducting nanotubes were identified, their positions were marked on PL, absorption and Raman spectra. Then metallic nanotubes were identified on absorption and Raman spectra according to the remaining spectral features, taking into account the possibility of overlapping with semiconducting nanotubes.

It has to be noted that this approach works well for small diameter SWCNT (at or below  $\sim 1.1$  nm), and becomes exceedingly unreliable for larger nanotubes, for several reasons. First, interband transition energies of the larger nanotubes are closer to each other due to approximate  $E_{ii} \sim 1/d$

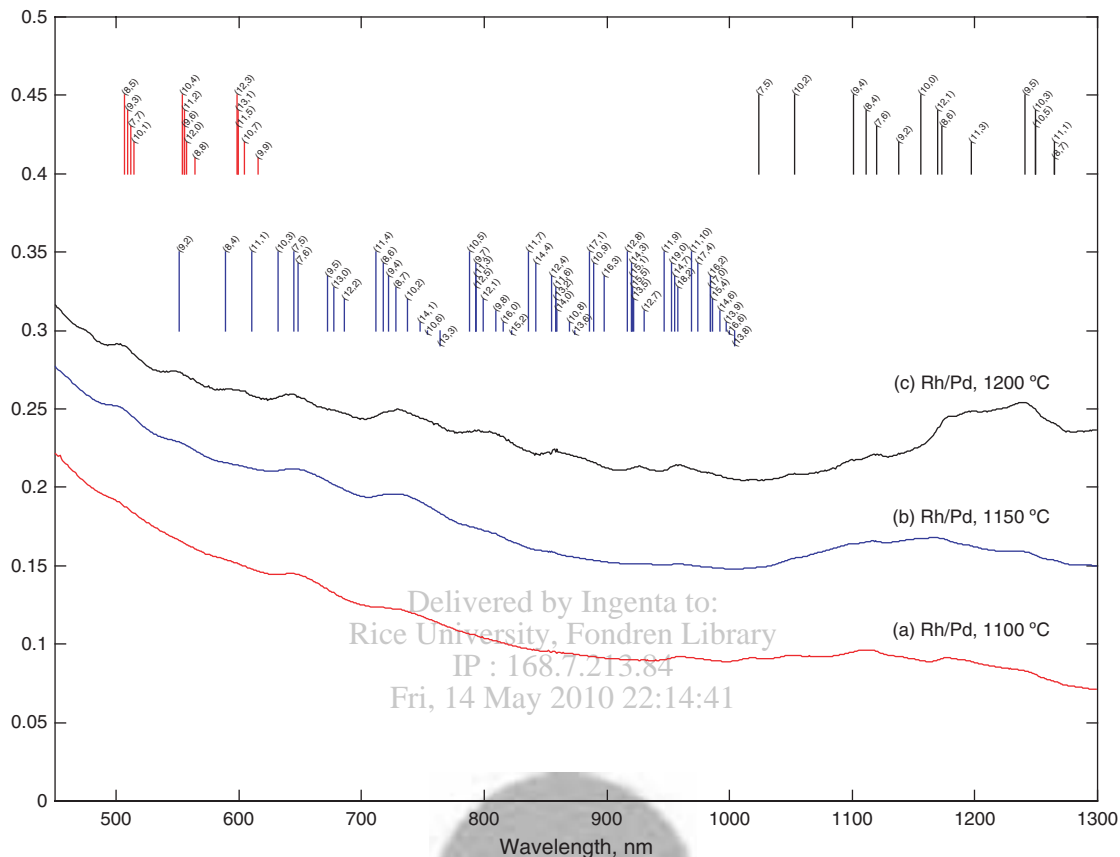


**Fig. 2.** UV-Vis-NIR absorption spectra of SWCNT samples produced on Rh/Pd catalyst at (a) 1100 °C, (b) 1150 °C and (c) 1200 °C. Metallic  $M_{11}$  transition are marked in red, semiconducting  $S_{22}$  in blue and  $S_{11}$  in black.

relationship between energies and diameter, and become impossible to resolve. This effect can be clearly seen on absorption spectra of the Co/Ni 1100 °C sample (Fig. 1), where the low energy side of the  $S_{22}$  hump can be identified

with more than a dozen semiconducting nanotube types, but their spectral features coalesce into a broad shoulder. The numerous larger tubes identified on the chiral map of this sample (Fig. 13) are therefore possible assignments of

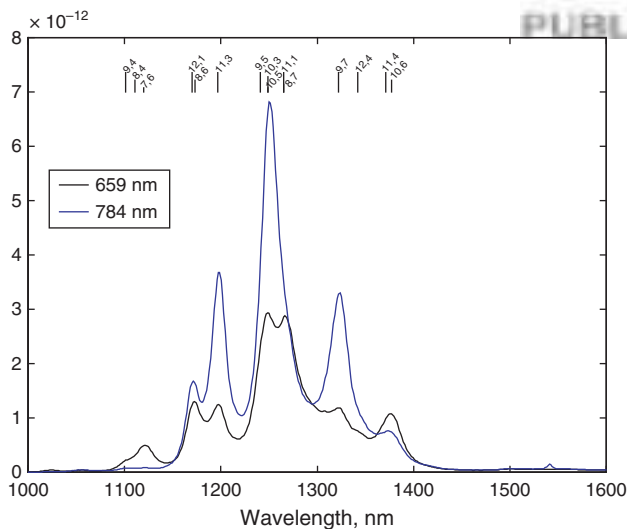


**Fig. 3.** Photoluminescence spectra of SWCNT sample produced on Co/Ni catalyst at 900 °C. Black—659 nm excitation, blue—784 nm excitation.  $S_{11}$  transitions are marked on top.

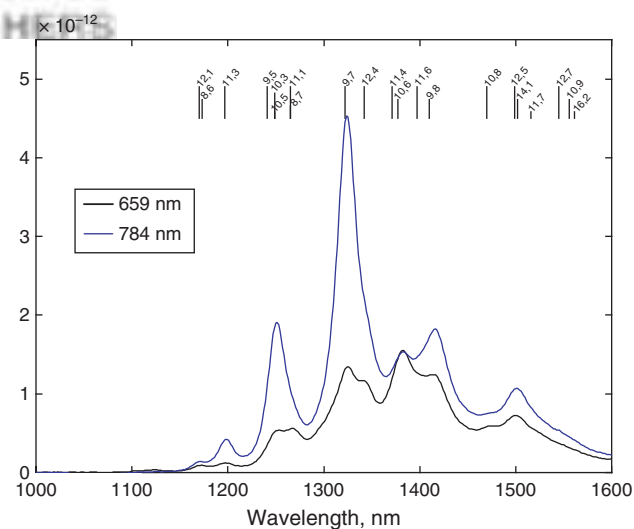


**Fig. 4.** Photoluminescence spectra of SWCNT sample produced on Co/Ni catalyst at 1000 °C. Black—659 nm excitation, blue—784 nm excitation.  $S_{11}$  transitions are marked on top.

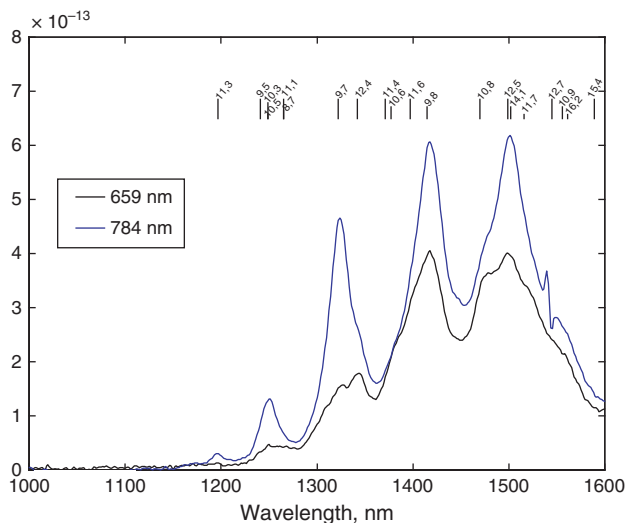


**Fig. 5.** Photoluminescence spectra of SWCNT sample produced on Co/Ni catalyst at 1100 °C. Black—659 nm excitation, blue—784 nm excitation.  $S_{11}$  transitions are marked on top.

nanotube structures that fall within this absorption range. It is impossible to truly discriminate among them, and therefore all these structures are taken into account. Same is true even for smaller diameter tubes, since transition energies tend to group closely together (especially for small diameter metallic tubes). This emphasizes that there is less certainty in the  $(n, m)$  assignments made from absorption data than in those made from PL and Raman. Second, large diameter nanotubes can not be detected on PL spectra due to limited wavelength range of the Nanospectralyzer and transmission cut-off in  $D_2O$ . Even detectable nanotubes with PL emission frequencies close to the 1600 nm detector limit have transition energies close to each other and are

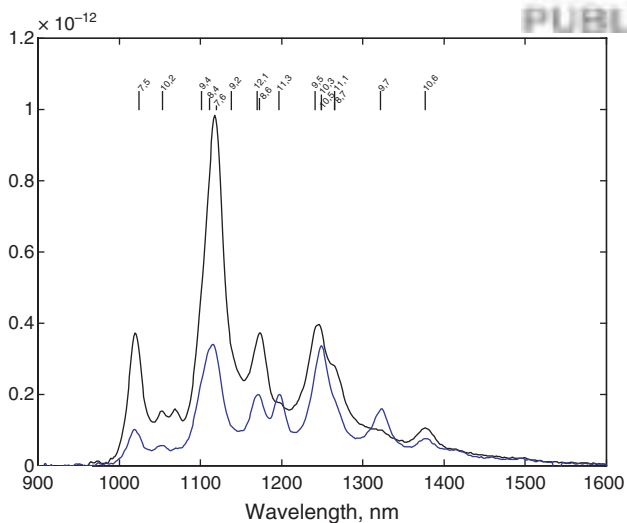


**Fig. 6.** Photoluminescence spectra of SWCNT sample produced on Rh/Pd catalyst at 1100 °C. Black—659 nm excitation, blue—784 nm excitation.  $S_{11}$  transitions are marked on top.

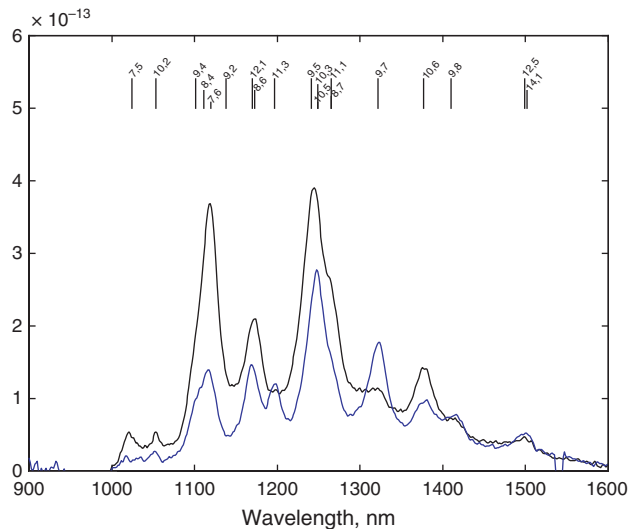


**Fig. 7.** Photoluminescence spectra of SWCNT sample produced on Rh/Pd catalyst at 1150 °C. Black—659 nm excitation, blue—784 nm excitation.  $S_{11}$  transitions are marked on top.

difficult to resolve on PL spectra. Similar difficulties with PL of large diameter nanotubes were noted in Ref. [36]. Third,  $S_{22}$  transitions of these nanotubes are too far from the 785 nm Raman excitation to be detected, while excitation on the  $S_{33}$  transition with 514 nm laser only detects three distinct nanotubes. The latter problem can be overcome by using a tunable Raman, however tunable Raman instruments are rare, and experiments are difficult, time consuming, and require careful intensity calibration.

Attempts to fit absorption and PL spectra with a number of Lorentzian lines corresponding to nanotube types present in the samples turned out to be inconclusive. The

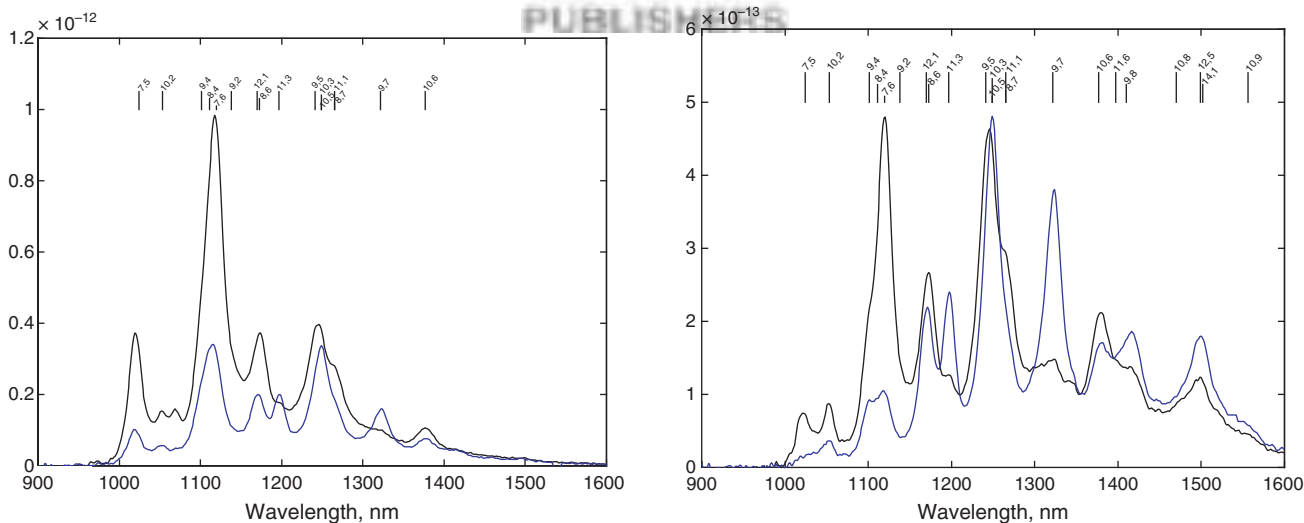


**Fig. 8.** Photoluminescence spectra of SWCNT sample produced on Rh/Pd catalyst at 1200 °C. Black—659 nm excitation, blue—784 nm excitation.  $S_{11}$  transitions are marked on top.

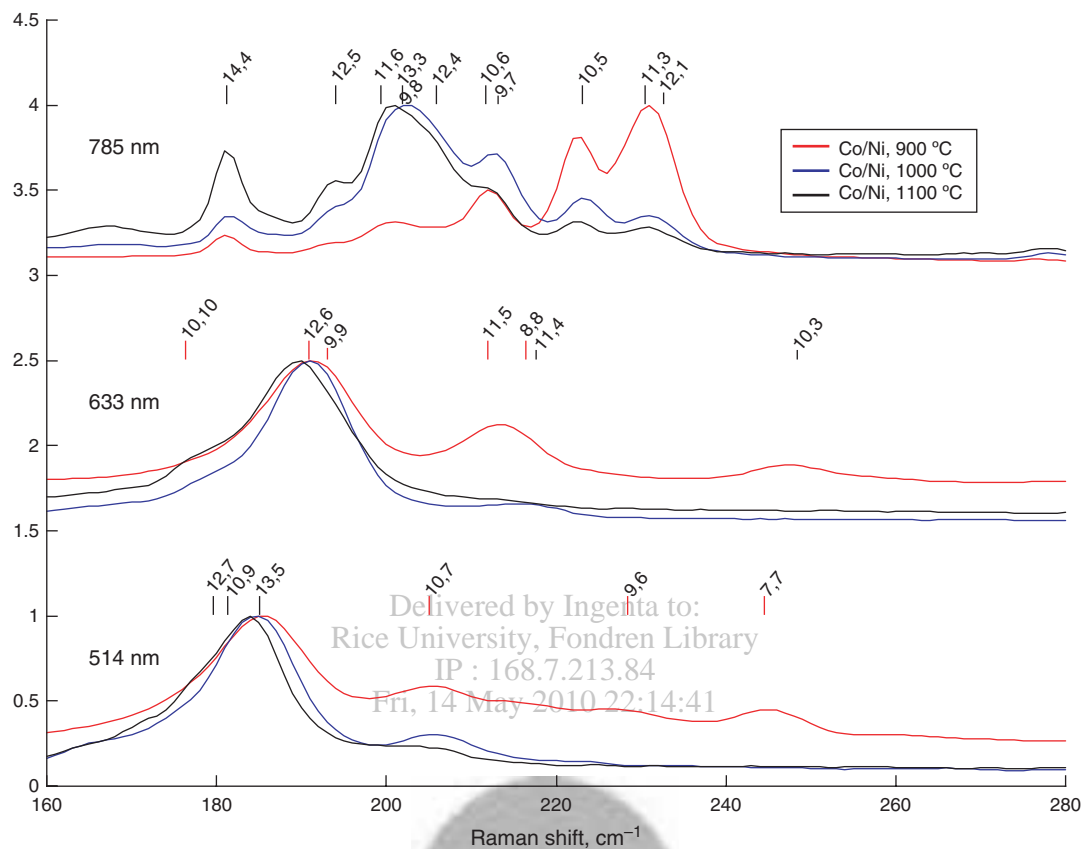


**Fig. 9.** Raman RBM spectra of SWCNT samples produced on Co/Ni catalyst. Red—900 °C, blue—1000 °C, black—1100 °C. (a)—785 nm excitation, (b)—633 nm excitation, (c)—514 nm excitation. Metallic SWCNT RBM frequencies are marked in red, semiconducting—in black.

precise transition energies are sensitive to the environment, and small change in the transition energies of two closely overlapping peaks led to large variations in the respective peak intensities. Apart from that, the fitting of the absorption spectra was found to be sensitive to the variations in the background subtraction. Even if reliable Lorentzian fits could be achieved, the relationships between nanotube concentration and intensity of its spectral features are not known accurately, and are known to vary quite a bit among nanotube types.<sup>37–40</sup> Therefore, nanotube populations were simply expressed as “major” nanotube types with very strong spectral features and “minor” nanotube types with weaker but definitely detectable spectral features.

The results of the population analyses are shown on Figures 11–16. Nanotubes present on absorption spectrum are marked with red hexagons, PL spectra—blue hexagons, and Raman spectra—green hexagons. Thick hexagons represent major SWCNT types, and thin hexagons—minor SWCNT types.

The increase in the average diameters and widths of diameter distributions at higher temperatures, noted above from the shapes and positions of the absorption and PL spectral features, is seen on these  $(n, m)$  maps as well. However,  $(n, m)$  maps also reveal the effect the temperature has on the nanotubes’ chiral angles.

In case of Co/Ni 900 °C sample, major nanotube types cluster in the 12–30° chiral angle range, most major types being either armchair metals ((7, 7), (8, 8) and (9, 9)) or very close to 30° ((8, 7), (9, 7), (9, 8)). The major types that are not armchairs ((9, 6), (10, 5), (11, 3)) all have very close diameters in 1.00–1.05 nm range. As the temperature is increased to 1000 °C, the nanotube population broadens and shifts towards larger diameters, with major types covering 1.05–1.20 nm range. Interestingly, chiral angles shift away from the 30°, with only (9, 9) armchair tube present. As the temperature is further increased to 1100 °C, the nanotube population broadens dramatically, with the major types covering 1.15–1.35 nm diameter range and 4–30° chiral angle range. The tendency towards close to armchair chiralities remains, while only one major armchair type (9, 9) is detected, with very little (10, 10) present as well.

The picture with Rh/Pd samples is quite different. At 1100 °C Rh/Pd catalyst produced somewhat broader diameter distribution compared to Co/Ni 900 °C sample, in the 0.85–1.05 nm diameter range. There is less preference towards close-to-armchair structures, and chiral angles of the major types cover broader range, 5–30°. As the temperature is increased to 1150 and then to 1200 °C, small nanotubes that were present at 1100 °C do not disappear

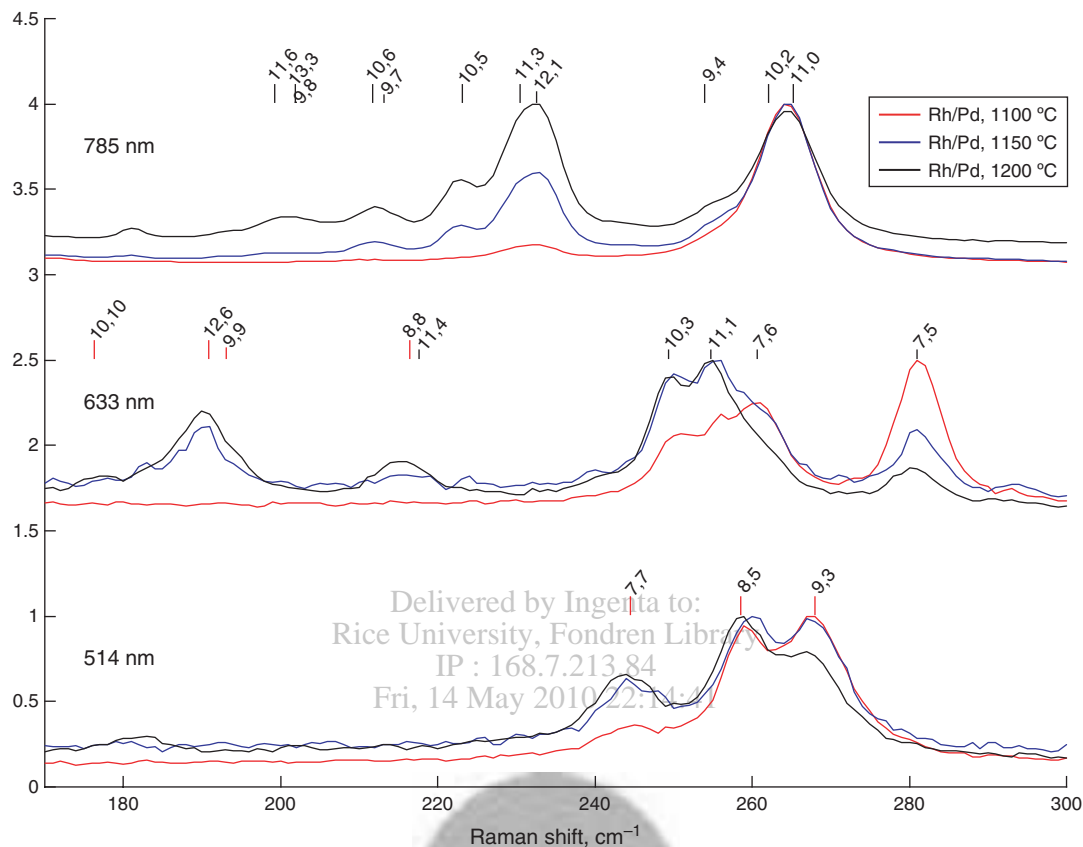


**Fig. 10.** Raman RBM spectra of SWCNT samples produced on Rh/Pd catalyst. Red—1100 °C, blue—1150 °C, black—1200 °C. (a)—785 nm excitation, (b)—633 nm excitation, (c)—514 nm excitation. Metallic SWCNT RBM frequencies are marked in red, semiconducting—in black.

completely as is the case with Co/Ni catalyst, but rather the nanotube population is broadened towards larger diameter tubes, reaching 0.85–1.2 nm diameter range.

It is difficult to compare these populations to that in standard PLV nanotubes produced with Co/Ni catalyst at 1200 °C. Since standard PLV nanotubes have diameters in the  $1.4 \pm 0.3$  nm range,<sup>12,29</sup> the population analysis in these is not truly possible via spectroscopy for reasons stated above, and has not been attempted. Recent electron beam diffraction data shows broad chiral angle distribution somewhat skewed towards 30°,<sup>41</sup> which suggests a broad nanotube population skewed towards armchair types.

An important observation can be made: in all Rh/Pd samples, and in Co/Ni 900 °C sample, larger diameters are clearly associated with larger chiral angles. This trend is consistent with a simple picture of the energy balance of a nanotube nuclei proposed in Ref. [42]. As the nuclei size changes, the strain energy of a curved graphene sheet is balanced by the energy of the open graphene edge. A decrease in the edge energy will cause an increase in the nucleus diameter<sup>43</sup> for a fixed number of carbon atoms. It has been estimated that an armchair edge is ~15% more stable compared to a zig-zag edge (12.14 vs. 10.31 eV/nm) due to formation of partial triple bonds between one-coordinated carbon atoms on armchair edge.<sup>44</sup> Therefore,

nuclei structures that are closer to armchair configuration will tend to nucleate nanotubes of the largest diameter. Note that this picture is largely oversimplified, as nanotube nuclei probably do not reach any meaningful thermal equilibrium in a rapidly expanding and cooling plume of carbon clusters. However, it does point in the right direction.

The temperature dependence of the average nanotube diameter can be explained by changes in the cooling rate of the ablated carbon species. As the carbon vapor plume expands and cools down, the nanotube structure becomes kinetically fixed when the temperature is not high enough to allow rearrangement of the carbon atoms.<sup>46–48</sup> Expansion into colder buffer gas increases the cooling rate, and will lead to nanotube nuclei size being fixed earlier in time, and therefore to smaller nanotube diameters. Smaller nanotube diameters observed with Rh/Pd catalyst at comparable temperatures are also consistent with this picture. Rh/Pd catalyst has lower saturated vapor pressure compared to Co/Ni, and therefore will start to adsorb on the graphitic nanotube/fullerene precursors to form nanotube nuclei earlier in time. This leads to earlier nucleation and smaller nanotube diameters as well. Earlier nucleation with Rh/Pd may also explain the noted behavior of the SWCNT type population with increase in temperature.

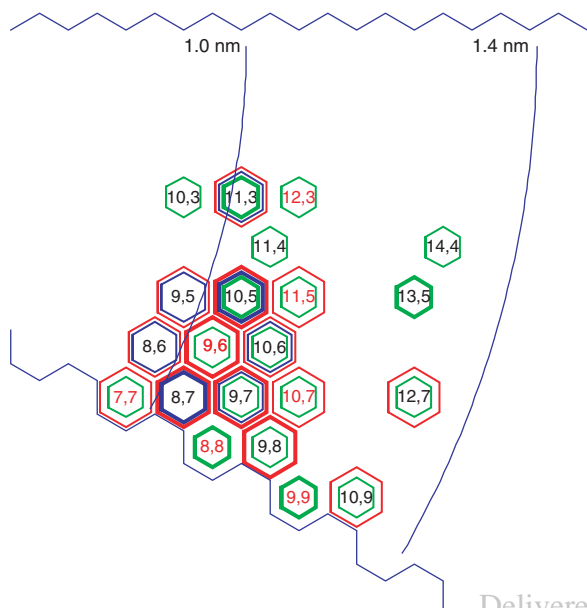


**Fig. 11.** Population map of the SWCNT sample produced on Co/Ni catalyst at 900 °C. Nanotubes present on absorption spectrum are marked with red hexagons, PL spectra—blue hexagons, and Raman spectra—green hexagons. Thick hexagons represent major SWCNT types, and thin hexagons—minor SWCNT types.

The decrease in the intensity of the absorption features with respect to background (Figs. 1 and 2) implies that SWCNT purity decreases noticeably with decrease in the temperature, and this effect is more pronounced for Rh/Pd

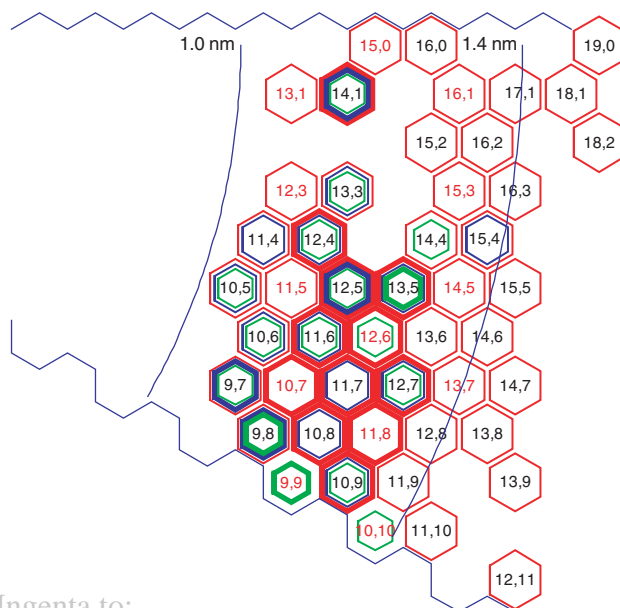


**Fig. 13.** Population map of the SWCNT sample produced on Co/Ni catalyst at 1200 °C. Nanotubes present on absorption spectrum are marked with red hexagons, PL spectra—blue hexagons, and Raman spectra—green hexagons. Thick hexagons represent major SWCNT types, and thin hexagons—minor SWCNT types.

catalyst. However, the ablation rate (quantity of material collected per hour) has only showed weak dependence on the oven temperature for both catalysts, decreasing by ~20% at the lowest temperatures. This implies that purity

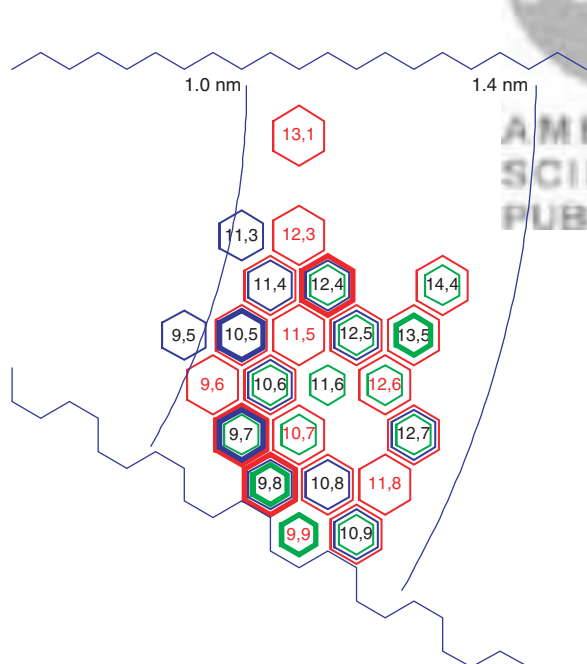


**Fig. 12.** Population map of the SWCNT sample produced on Co/Ni catalyst at 1000 °C. Nanotubes present on absorption spectrum are marked with red hexagons, PL spectra—blue hexagons, and Raman spectra—green hexagons. Thick hexagons represent major SWCNT types, and thin hexagons—minor SWCNT types.

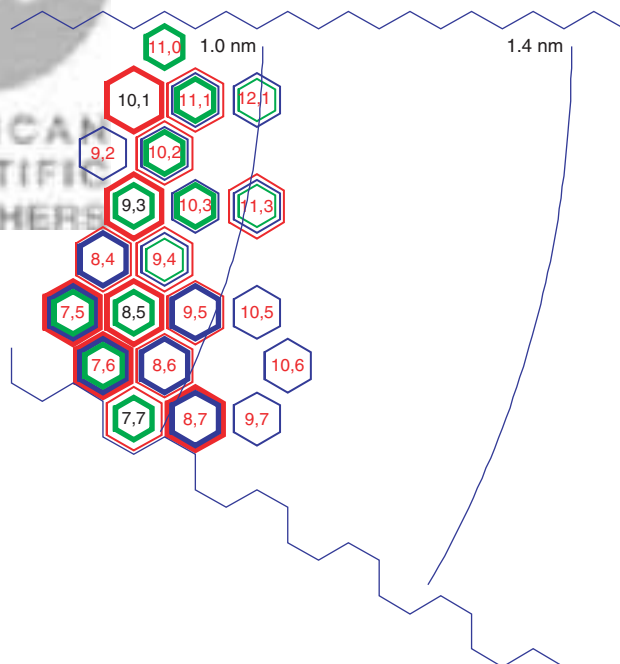


**Fig. 14.** Population map of the SWCNT sample produced on Rh/Pd catalyst at 1100 °C. Nanotubes present on absorption spectrum are marked with red hexagons, PL spectra—blue hexagons, and Raman spectra—green hexagons. Thick hexagons represent major SWCNT types, and thin hexagons—minor SWCNT types.

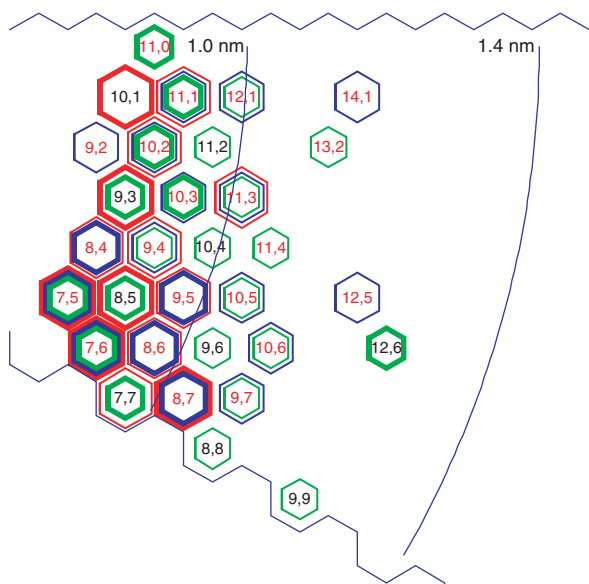


**Fig. 15.** Population map of the SWCNT sample produced on Rh/Pd catalyst at 1150 °C. Nanotubes present on absorption spectrum are marked with red hexagons, PL spectra—blue hexagons, and Raman spectra—green hexagons. Thick hexagons represent major SWCNT types, and thin hexagons—minor SWCNT types.

decrease is mostly a result of slower/less efficient nanotube growth that occurs long past nucleation, when their temperature equilibrates with that of the buffer gas. We can not exclude a possibility that higher cooling rates negatively

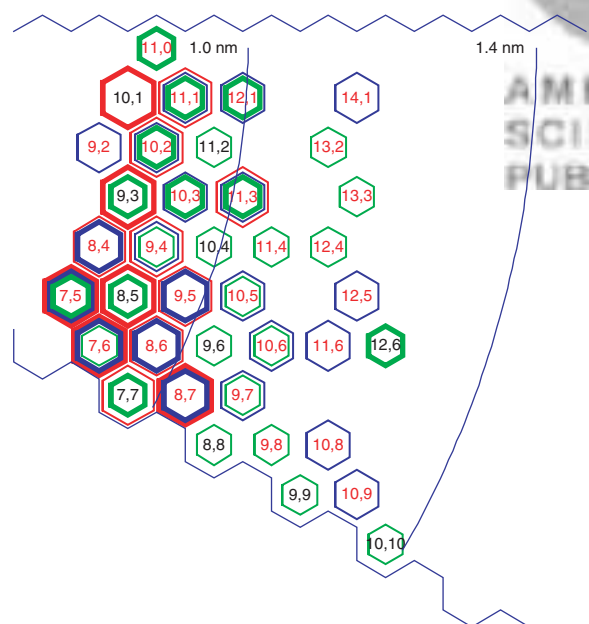


**Fig. 16.** Population map of the SWCNT sample produced on Rh/Pd catalyst at 1200 °C. Nanotubes present on absorption spectrum are marked with red hexagons, PL spectra—blue hexagons, and Raman spectra—green hexagons. Thick hexagons represent major SWCNT types, and thin hexagons—minor SWCNT types.

affect the efficiency of nanotube nucleation as well, and some of the purity decrease is caused by this.

Another interesting observation was made with respect to Raman and absorption intensities of armchair nanotubes. Armchair nanotubes ((7, 7), (8, 8) and (9, 9)) present in the Co/Ni 900 °C sample all have easily identifiable Raman peaks (Fig. 9). The absorption peaks at 550 and 600 nm that are in the vicinity of (8, 8) and (9, 9) transitions (Fig. 1) are much better identified with (9, 6) and (10, 7), that have closer transition energies and clear Raman signatures as well. Therefore, the optical absorption by (8, 8) and (9, 9) armchair tubes is very small if nonexistent, in agreement with.<sup>35</sup> On the contrary, the absorption peak at 505 nm clearly belongs to (7, 7) tube, since all chiral metallic tubes with close transition energies ((8, 5), (9, 3) and (10, 1)) are absent on Raman RBM spectra. It can be concluded that optical absorption by (7, 7) tube is “regular,” i.e., similar to chiral metallics, while the absorption by (8, 8) and (9, 9) is vanishingly small. This behavior of (7, 7) tube goes against the symmetry arguments put forward in Ref. [37], and the reasons for this are not clear and beyond the scope of this work.

## 4. CONCLUSIONS

Single-wall carbon nanotubes were produced with Co/Ni catalyst at 900, 1000 and 1100 °C temperatures, and with Rh/Pd catalyst at 1100, 1150 and 1200 °C temperatures. Nanotube type populations were studied by absorption, photoluminescence and Raman spectroscopies. The samples prepared with both catalysts at lowest temperatures have rather narrow type distributions compared to more common HiPco samples. Therefore, they appear quite attractive as a starting material for nanotube type separation experiments. Considering noticeably higher yield and lower cost, as well as narrower type population, SWCNTs synthesized with Co/Ni catalyst at 900 °C are preferred. Interestingly, in samples produced at lower temperatures, larger nanotube diameters tend to be associated with larger chiral angles.

**Acknowledgments:** Authors would like to acknowledge financial support from NASA under contract #NNJ05HI05C and from State of Texas, Space Act Agreement #SAA-AT-07-021 (RAN 0798) (UTA07-099). Authors thank R. Bruce Weisman of Rice University for access to the Nanospectralyzer for photoluminescence measurements.

## References and Notes

1. M. Anantram and F. Leonard, *Rep. Prog. Phys.* 69, 507 (2006).
2. P. Avouris, Z. H. Chen, and V. Perebeinos, *Nature Nanotechnol.* 2, 605 (2007).
3. E. T. Thostenson, Z. F. Ren, and T. W. Chou, *Compos. Sci. Technol.* 61, 1899 (2001).

4. B. K. Kaushik, S. Goel, and G. Rauthan, *Microelectron. Int.* 24, 53 (2007).
5. B. Mahar, C. Laslau, R. Yip, and Y. Sun, *IEEE Sens. J.* 7, 266 (2007).
6. J. C. Charlier, X. Blase, and S. Roche, *Rev. Mod. Phys.* 79, 677 (2007).
7. T. Guo, P. Nikolaev, A. Thess, D. T. Colbert, and R. E. Smalley, *Chem. Phys. Lett.* 243, 49 (1995).
8. T. W. Ebbesen and P. M. Ajayan, *Nature* 358, 220 (1992).
9. P. Nikolaev, M. J. Bronikowski, R. K. Bradley, F. Rohmund, D. T. Colbert, K. A. Smith, and R. E. Smalley, *Chem. Phys. Lett.* 313, 91 (1999).
10. G. Lolli, L. Zhang, L. Balzano, N. Sakulchaicharoen, Y. Tan, and D. E. Resasco, *J. Phys. Chem. B* 110, 2108 (2006).
11. Y. Miyauchi, S. Chiashi, Y. Murakami, Y. Hayashida, and S. Maruyama, *Chem. Phys. Lett.* 387, 198 (2004).
12. A. G. Rinzler, J. Liu, H. Dai, P. Nikolaev, C. B. Huffman, F. J. Rodriguez-Macias, P. J. Boul, A. H. Lu, D. Heymann, D. T. Colbert, R. S. Lee, J. E. Fischer, A. M. Rao, P. C. Eklund, and R. E. Smalley, *App. Phys. A* 67, 29 (1998).
13. J. Hinkov, M. Grand, L. de la Chapelle, S. Farhat, C. D. Scott, P. Nikolaev, V. Pichot, P. Launois, J. Y. Mevellec, and S. Lefrant, *J. App. Phys.* 95 2029 (2004).
14. R. L. Carver, H. Q. Peng, A. K. Sadana, P. Nikolaev, S. Arepalli, C. D. Scott, W. E. Billups, R. H. Hauge, and R. E. Smalley, *J. Nanosci. Nanotechnol.* 5, 1035 (2005).
15. S. M. Bachilo, M. S. Strano, C. Kittrell, R. H. Hauge, R. E. Smalley, and R. B. Weisman, *Science* 298, 2361 (2002).
16. M. C. Hersam, *Nature Nanotechnol.* 3, 387 (2008).
17. A. A. Green and M. C. Hersam, *Mater. Today* 10, 59 (2007).
18. M. S. Arnold, S. I. Stupp, and M. C. Hersam, *Nano Lett.* 5, 713 (2005).
19. M. S. Arnold, A. A. Green, J. F. Hulvat, S. I. Stupp, and M. C. Hersam, *Nature Nanotechnol.* 1, 60 (2006).
20. S. Toyoda, Y. Yamaguchi, M. Hiwatashi, Y. Tomonari, H. Murakami, and N. Nakashima, *Chem.—Asian J.* 2, 145 (2007).
21. S.-Y. Ju, J. Doll, I. Sharma, and F. Papadimitrakopoulos, *Nature Nanotechnol.* 3, 356 (2008).
22. M. Zheng, A. Jagota, E. D. Semke, B. A. Diner, R. S. Mclean, S. R. Lustig, R. E. Richardson, and N. G. Tassi, *Nature Mater.* 2, 338 (2003).
23. M. Zheng, A. Jagota, M. S. Strano, A. P. Santos, P. Barone, S. G. Chou, B. A. Diner, M. S. Dresselhaus, R. S. Mclean, G. B. Onoa, Ge. G. Samsonidze, E. D. Semke, M. Usrey, and D. J. Walls, *Science* 302, 1545 (2003).
24. T. Tanaka, H. Jin, Y. Miyata, and H. Kataura, *Appl. Phys. Exp.* 1, 114001 (2008).
25. T. Tanaka, H. Jin, Y. Miyata, S. Fujii, H. Suga, Y. Naitoh, T. Minari, T. Miyadera, K. Tsukagoshi, and H. Kataura, *Nano Lett.* ASAP (web date February 25, 2009).
26. D. H. Shin, J.-E. Kim, H. C. Shim, J.-W. Song, J.-H. Yoon, J. Kim, S. Jeong, J. Kang, S. Baik, and C.-S. Han, *Nano Lett.* 8, 4380 (2008).
27. M. J. Mendes, H. K. Schmid, and M. Pasquali, *J. Phys. Chem. B* 112, 7467 (2008).
28. S. Suzuki, N. Asai, H. Kataura, and Y. Achiba, *Eur. Phys. J. D* 43, 143 (2007).
29. S. Arepalli, W. A. Holmes, P. Nikolaev, V. G. Hadjiev, and C. D. Scott, *J. Nanosci. Nanotechnol.* 4, 762 (2004).
30. S. Arepalli and C. Scott, *Chem. Phys. Lett.* 302, 139 (1999).
31. S. Arepalli, P. Nikolaev, W. Holmes, and C. D. Scott, *Appl. Phys. A* 70, 125 (2000).
32. S. Arepalli, *J. Nanosci. Nanotechnol.* 4, 317 (2004).
33. B. J. Landi and R. P. Raffaele, *J. Nanosci. Nanotechnol.* 7, 883 (2007).
34. R. B. Weisman and S. M. Bachilo, *Nano Lett.* 3, 1235 (2003).
35. P. T. Araujo, S. K. Doorn, S. Kilina, S. Tretiak, E. Einarsson, S. Maruyama, H. Chacham, M. A. Pimenta, and A. Jorio, *Phys. Rev. Lett.* 98, 067401 (2007).
36. T. Okazaki, T. Saito, K. Matsuura, S. Ohshima, M. Yumura, Y. Oyama, R. Saito, and S. Iijima, *Chem. Phys. Lett.* 420, 286 (2006).
37. J. Jiang, R. Saito, A. Gruneis, G. Dresselhaus, and M. S. Dresselhaus, *Carbon* 42, 3169 (2004).
38. Y. Oyama, R. Saito, K. Sato, J. Jiang, Ge. G. Samsonidze, A. Gruneis, Y. Miyauchi, S. Maruyama, A. Jorio, G. Dresselhaus, and M. S. Dresselhaus, *Carbon* 44, 8739 (2006).
39. J. Jiang, R. Saito, K. Sato, J. S. Park, Ge. G. Samsonidze, A. Jorio, G. Dresselhaus, and M. S. Dresselhaus, *Phys. Rev. B* 75, 035405 (2007).
40. D. A. Tsybouski, J.-D. R. Rocha, S. M. Bachilo, L. Cognet, and R. B. Weisman, *Nano Lett.* 7, 3080 (2007).
41. H. Jiang, D. P. Brown, P. Nikolaev, A. G. Nasibulin, and E. I. Kauppinen, *Appl. Phys. Lett.* 93, 141903 (2008).
42. A. Thess, R. Lee, P. Nikolaev, H. J. Dai, P. Petit, J. Robert, C. H. Xu, Y. H. Lee, S. G. Kim, A. G. Rinzler, D. T. Colbert, G. E. Scuseria, D. Tomanek, J. E. Fischer, and R. E. Smalley, *Science* 273, 483 (1996).
43. The strain/edge energy of a nanotube nucleus (represented as a cylinder capped on one end by a hemifullerene) is  $E = E_c + E_r + E_e$ , where  $E_c$  is strain energy of the hemifullerene cap,  $E_r$  is strain energy of the cylindrical section, and  $E_e$  is energy of the open nanotube edge. The strain energy of a hemifullerene cap,  $E_c$ , is to a very good approximation independent of its radius.<sup>45</sup> The strain energy of the attached cylinder of radius  $R$  and length  $L$  is  $E_r = \epsilon_r LR$ , where  $\epsilon_r$  is bending stiffness of a graphene sheet,  $L$  is length of the cylinder, and  $R$  is tubulet radius. Finally, the energy stored in the dangling bonds at the open cylinder edge is  $E_e = 2\pi R \epsilon_e$ , where  $\epsilon_e$  is energy of the open edge per unit length. Minimization of the energy with respect to  $R$  for a fixed number of carbon atoms  $N$  yields  $R \sim (N\epsilon_r/\epsilon_e)^{1/3}$ . Therefore, decrease in the edge energy  $\epsilon_e$  will lead to increase in the diameter of a nanotube nucleus.
44. Y. H. Lee, S. G. Kim, and D. Tománek, *Phys. Rev. Lett.* 78, 2393 (1997).
45. D. Tomanek, W. Zhong, and E. Krastev, *Phys. Rev. B* 48, 15461 (1993).
46. C. D. Scott, S. Arepalli, P. Nikolaev, and R. E. Smalley, *Appl. Phys. A* 72, 573 (2001).
47. A. A. Puztzky, D. B. Geohegan, X. Fan, and S. J. Pennycook, *Appl. Phys. A* 70, 153 (2000).
48. A. A. Puztzky, H. Schittenhelm, Xu. Fan, M. J. Lance, L. F. Allard, Jr., and D. B. Geohegan, *Phys. Rev. B* 65, 245425 (2002).

Received: 28 February 2009. Revised/Accepted: 2 April 2009.